Available online at www.sciencedirect.com
ScienceDirect
Trans. Nonferrous Met. Soc. China 34(2024) 3662−3676

Transactions of Nonferrous Metals Society of China
www.tnmsc.cn

Mechanism of high temperature oxidation of Inconel 625 superalloy with various solution and ageing heat treatment processes

Jiang-kun FAN[1,2,3], Hong-ci YANG[1], Pei-zhe ZHANG[1], Jia-yu LI[1], Zhan-jie JING[1],
Fu-long CHEN[1,4], De-gui LIU[4], Bin TANG[1,2,3], Hong-chao KOU[1,2,3], Jin-shan LI[1,2,3]

1. State Key Laboratory of Solidification Processing, Northwestern Polytechnical University, Xi’an 710072, China;
2. National & Local Joint Engineering Research Center for Precision Thermoforming Technology of Advanced Metal Materials, Xi’an 710072, China;
3. Chongqing Innovation Center, Northwestern Polytechnical University, Chongqing 401135, China;
4. AVIC Manufacturing Technology Institute, Beijing 100024, China

Received 1 April 2023; accepted 7 November 2023

Abstract: The high-temperature oxidation behaviour of the Inconel 625 alloy at 950 °C was investigated after different ageing treatments. The effect of heat treatment on the oxidation behaviour of the alloy was analysed by characterizing the structure and elemental distribution before and after oxidation. The results reveal that the two ageing treatments at 650 °C for 500 h and at 750 °C for 400 h both reduced the oxidation mass gain. After oxidation at 950 °C, an outer Cr_2O_3 layer and inner Al_2O_3 are identified as the main oxidation products. Moreover, Nb_2O_5 and $\delta(Ni_3Nb)$ phases precipitated after oxidation. The ageing treatments cause the rapid generation of a dense Cr_2O_3 layer on the surface, which prevents the diffusion of oxygen into the matrix, reduce the Al_2O_3 inward growth depth, and improve the oxidation resistance of the alloy.

Key words: Inconel 625 alloy; ageing treatment; oxidation behaviour; oxidation film; kinetics

1 Introduction

Inconel 625 alloy is a Ni-based superalloy which is generally strengthened by solid-solution strengthening using Cr, Mo, Nb, and Fe [1−3]. It has good mechanical properties and high-temperature oxidation resistance and is widely used in petrochemical, aerospace, marine, power generation, and nuclear industries [4−6]. However, when used at high temperatures, de-alloying, surface spalling and even scale failure may occur due to the effects of high temperature oxidation [7−9], ultimately affecting the creep and tensile properties of the alloy [10]. VESEL et al [11] studied the growth of an oxide film on the Inconel 625 alloy and observed the formation of a 30 nm-thick NiO film on the alloy surface in a short time (less than 1 min). Subsequently, a layer of Cr_2O_3 was formed on the NiO film, and then crystalline cluster-like Nb_2O_5 was formed on the surface of the alloy. At higher temperatures, $NiCr_2O_4$ also precipitated at the interface between Cr_2O_3 and NiO phases. SHARIFITABAR et al [12] reported that dense Cr_2O_3 and Ni_3Nb phases were formed on the Inconel 625 alloy surface when it was heated at 800−1000 °C for 20 h. When the temperature was increased to 1100 °C, Ni_3Nb was oxidized to form $CrNbO_4$ at the oxide−alloy interface. The high resistance to high temperature oxidation of Inconel 625 alloy is due to chromium, which has a good affinity for oxygen and forms a stable protective oxide layer on the surface of the alloy [13,14], which hinders the diffusion behavior of the elements

---

Corresponding author: Jiang-kun FAN, Tel: +86-29-88460294, E-mail: jkfan@nwpu.edu.cn

DOI: 10.1016/S1003-6326(24)66632-X

during oxidation and improves the oxidation resistance of the alloy. SUN et al [15] reported that crushed intermittent Cr_2O_3 is difficult to protect the alloy and Cr_2O_3 oxides turn into poorly protected $Ni(Cr,Fe)_2O_4$ spinel phase. Then, the oxide layer expands inward and causes further oxidation. Therefore, the rapid generation of a dense Cr_2O_3 layer that is not easily detached is the key to improving the oxidation resistance of the alloy.

During heat treatment, the carbide, γ' phase, γ'' phase and δ phase of nickel-based superalloy undergo complex evolution, which affects the mechanical properties of the alloy. The microstructure changes caused by heat treatment will inevitably affect the oxidation properties of the alloy, but unfortunately there are few systematic studies at present. The effect of thermal post treatments consisting of heat treatment (HT), hot isostatic pressing (HIP), and combined HIP-HT on microstructure and oxidation behavior of 718 alloy manufactured by electron beam powder bed fusion (EB-PBF) technique was investigated [16]. The effect of δ phase characteristics on the oxidation resistance of alloy is significantly different. Both heat treatment and hot isostatic pressing improve the oxidation resistance of the alloy by reducing grain size, closing pores, and creating a more homogeneous microstructure. LIANG et al [17] found that heat treatment significantly improved the oxidation resistance of Ti−45Al−8Nb alloy, as evidenced by lower oxidation rates, smaller oxidation mass gain, and thinner oxide layer thickness. The improved oxidation resistance results from: (1) the transformation of the near-γ organization into a bidirectional phase weave after heat treatment, which improves the oxidation resistance; (2) the partial twin grain boundary replaces the high-angle grain boundary, which reduces the O^{2-} inward diffusion channel; (3) the formation of continuous $AlNb_2$ layer inhibits the O^{2-} diffusion into the matrix. TIAN et al [18] found that cyclic heat treatment also improved the oxidation resistance of TiAl alloys due to the elimination of the $\beta/B2$ phase, which has poor oxidation resistance, and the formation of a dense Nb, Mo-rich layer during oxidation. The effect of different microstructure characteristics and phase composition on oxidation mechanism needs to be further investigated.

As mentioned above, heat treatment as a necessary process will inevitably have an impact on the phase organization and elemental distribution of nickel-based superalloy. This in turn affects the oxidation resistance and performance of the alloy. In this work, the high-temperature oxidation behavior of the Inconel 625 alloy at 950 °C was investigated after different ageing treatments. The oxidation kinetics were analyzed by static mass gain method and the microstructural characterization of the alloy was characterized to describe the oxidation behavior and to elucidate the effect of aging treatment on the oxidation behavior. Aging treatment can effectively improve the oxidation resistance of the alloy at high temperatures. The oxidation mechanism of different stages of oxidation and the influence of γ'' and δ phases were revealed. It is believed that the conclusion and mechanism of the manuscript can provide new ideas for the microstructure and oxidation resistance design of these superalloys.

2 Experimental

In this study, rolled and annealed Inconel 625 plates of 5 mm in thickness were used, and their chemical composition is shown in Table 1. 10 mm × 10 mm × 5 mm specimens were first obtained by wire electrical discharge machining. Then, three different heat treatment states were obtained by different heat treatment methods: (1) heating at 1100 °C for 60 h (solution treatment), (2) heating at 1100 °C for 1 h followed by aging at 650 °C for 500 h, and (3) heating at 1100 °C for 1 h followed by aging at 750 °C for 400 h.

High-temperature oxidation experiments were conducted in a high-temperature chamber resistance furnace to study the surface mass gain kinetics of the alloy using the discontinuous mass gain method with reference to GB/T 13303-91. The heat-treated specimens were pre-ground on $240^\#$, $400^\#$, $800^\#$, $1200^\#$, $1500^\#$, $2000^\#$ and $3000^\#$ sandpaper to exclude the effect of roughness on the high-temperature oxidation behavior of the alloy. The specimens were degreased with acetone before the oxidation experiment and then cleaned with alcohol and waited for the specimens to dry. The samples were taken out at 1, 6, 12, 24, 50, 100, 125, 150 and 200 h, and weighed with an electronic balance with an accuracy of 0.1 mg. The high temperature oxidation kinetic curves were plotted according to the mass gain to study the oxidation rate and oxidation resistance of the alloy. The surface and cross-sectional morphology of the oxide layer and the distribution of elements in micro-regions were investigated using X-ray diffraction (XRD), scanning electron microscopy (SEM) and electron probe X-ray microanalysis (EPMA) to probe the phase composition of the oxide film and the formation and growth of the oxide products. The phase organization of the alloy after heat treatment and the distribution of elements were obtained using transmission electron microscopy (TEM) and EPMA as a way to investigate the effect of heat treatment on the oxidation behavior.

Table 1 Chemical composition of Inconel 625 superalloy (wt.%)

Ni	Cr	Mo	Nb	Fe	Al
60.74	21.71	8.93	3.32	4.22	0.52

Si	C	Ta	Ti	Mn
0.41	0.040	<0.01	0.21	0.41

3 Results and discussion

3.1 Oxidation kinetics

The isothermal oxidation kinetics curves of the three different heat treatment specimens oxidized at 950 °C in air are shown in Fig. 1(a). The three different curves exhibited similar shape characteristics, indicating that the oxidation mechanism of the Inconel 625 alloy did not change after the ageing treatment. The trend of oxidation mass gain was similar for all three specimens, with a rapid increase in mass during the initial period of oxidation and a subsequent slowdown in mass gain. In the initial period of high-temperature oxidation (0−24 h), oxygen atoms were adsorbed to the alloy surface to form oxygen ions, which rapidly reacted with the metal cations of the alloy, resulting in the rapid change in the surface quality. As the initially formed surface oxide layer hindered direct contact between the alloy matrix and oxygen in the air, further oxidation relied on the diffusion of elements, resulting in the significant reduction of the oxidation rate. After 200 h of oxidation, the mass increase of the two ageing alloys was 0.43 mg/cm^2 (650 °C, 500 h) and 0.4 mg/cm^2 (750 °C, 400 h), respectively, which were smaller than that of the solid-solution specimen (0.52 mg/cm^2), indicating that the ageing state has better oxidation resistance relative to the solid-solution state.

The oxidation kinetics during the isothermal oxidation of the alloy can be expressed by

$$\Delta m/A=kt^n \tag{1}$$

where $\Delta m/A$ is the mass gain per unit area, t is the oxidation time, k is the oxidation rate constant, and n is the rate exponent that determines the rate law. The n and k values can be determined by taking logarithms on both sides of Eq. (1) to convert it into a linear form as Eq. (2):

$$\lg(\Delta m/A)=\lg k+n\lg t \tag{2}$$

The reciprocal slope of the $\lg(\Delta m/A)$ vs $\lg t$ plot gives the n value, and Fig. 1(b) shows the double logarithmic plots of the mass gain with time at different temperatures.

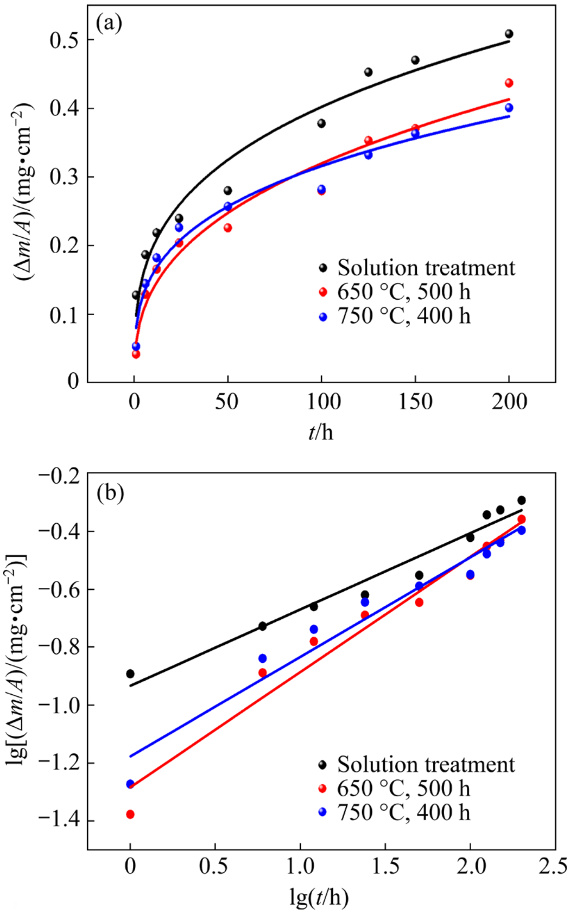

Fig. 1 Isothermal oxidation kinetics curves (a) and double logarithmic plots (b) of samples subjected to different heat treatments

Table 2 shows the oxidation rate constant (k) and the oxidation reaction index (n) values of the alloys subjected to different heat treatments. The oxidation mass gain index of the solid-solution alloy was 0.26, while the oxidation mass gain indices of the alloys aged at 650 °C for 500 h and 750 °C for 400 h were 0.39 and 0.34, respectively. The oxidation mass gain indices of the heat-treated alloys were between 0 and 0.5, which implied that the high-temperature oxidation process was controlled by elemental diffusion.

Table 2 Oxidation rate constant (*k*) and oxidation reaction index (*n*) of Inconel 625 alloy after different heat treatments

Heat treatment	*k*	*n*
Solution treatment	1.17×10^{-4}	0.26
650 °C, 500 h	6.61×10^{-5}	0.39
750 °C, 400 h	5.25×10^{-5}	0.34

3.2 Thermodynamics of oxides

Table 1 shows that the main elements in the Inconel 625 alloy that may participate in the high-temperature oxidation reaction are Ni, Cr, Mo, Nb, Fe, and Al. The following oxidation reactions may occur at elevated temperatures [19,20]:

$$2\mathrm{Ni(s)}+\mathrm{O_2(g)}=2\mathrm{NiO(s)},\ \Delta G_{\mathrm{NiO}}=-488+0.188T \tag{3}$$

$$4/3\mathrm{Cr(s)}+\mathrm{O_2(g)}=2/3\mathrm{Cr_2O_3(s)},\ \Delta G_{\mathrm{Cr_2O_3}}=-752+0.182T \tag{4}$$

$$\mathrm{Mo(s)}+\mathrm{O_2(g)}=\mathrm{MoO_2(s)},\ \Delta G_{\mathrm{MoO_2}}=-578+0.170T \tag{5}$$

$$4/5\mathrm{Nb(s)}+\mathrm{O_2(g)}=2/5\mathrm{Nb_2O_5(s)},\ \Delta G_{\mathrm{Nb_2O_5}}=-755+0.170T \tag{6}$$

$$4/3\mathrm{Al(s)}+\mathrm{O_2(g)}=2/3\mathrm{Al_2O_3(s)},\ \Delta G_{\mathrm{Al_2O_3}}=-1112.7+0.209T \tag{7}$$

$$3/2\mathrm{Fe(s)}+\mathrm{O_2(g)}=1/2\mathrm{Fe_3O_4(s)},\ \Delta G_{\mathrm{Fe_3O_4}}=-558.5+0.173T \tag{8}$$

Figure 2 shows the Gibbs free energy change of the formation of various oxides at different temperatures; the plots represent the standard free energy change of the oxidation reaction as a function of temperature, representing the thermodynamic driving force for the oxidation of each element. The Gibbs free energies for the formation of various oxides at different temperatures are all negative, indicating that all the oxidation reactions can proceed spontaneously at high temperatures. The order of the ΔG value of the different oxides is $\Delta G_{\mathrm{Al_2O_3}}<\Delta G_{\mathrm{Nb_2O_5}}<\Delta G_{\mathrm{Cr_2O_3}}<\Delta G_{\mathrm{MoO_2}}<\Delta G_{\mathrm{Fe_3O_4}}<\Delta G_{\mathrm{NiO}}$. As Al_2O_3 has the lowest Gibbs free energy change, it is the easiest to form at high temperatures. The driving forces for the formation of Cr_2O_3 and Nb_2O_5 are also high, whereas Ni, Fe, and Mo are expected to be relatively stable. The formation of Fe_3O_4, NiO and MoO_2 was not detected in subsequent work because the surface oxygen anions rapidly reacted with Cr to form a dense oxide film owing to the high content of Cr, and the oxide layer of Cr hindered the inward diffusion of oxygen anions and reduced the partial pressure of internal oxygen, thus preventing the generation of Fe_3O_4, NiO and MoO_2. Instead, Al is oxidized owing to its lowest Gibbs free energy change, despite its lower content.

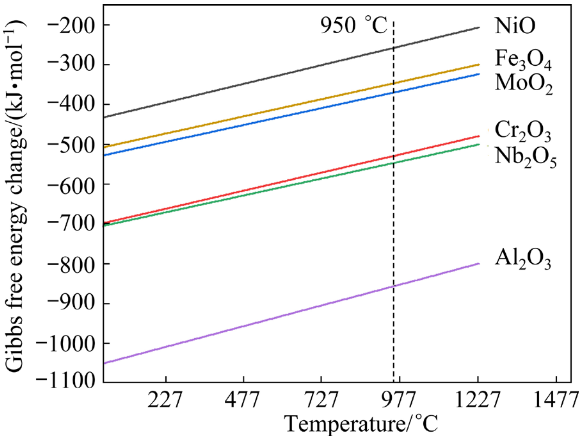

Fig. 2 Gibbs free energy change of formation of various oxides at different temperatures

3.3 Surface oxide products

The XRD patterns of the surface oxide scales of the differently heat-treated alloys after 1, 24, and 200 h of oxidation at 950 °C are shown in Fig. 3. The three different specimens exhibited similar oxidation product types after different oxidation time. The oxides formed after 1 h of oxidation are shown in Fig. 3(a); the alloy samples primarily consisted of Cr_2O_3, Al_2O_3, and the matrix during the initial period of oxidation. The diffraction peak of the matrix was evident after 1 h of oxidation, indicating that a continuous oxide was not formed on the surface in the initial stage. The diffraction peaks of Nb_2O_5 and the δ phase (Ni_3Nb) were observed after 24 h of oxidation, as shown in Fig. 3(b). Figure 3(c) shows the XRD pattern of the Inconel 625 alloy after oxidation at 950 °C for 200 h. The type of oxidation products remains the same within 24−200 h. The diffraction peaks of Cr_2O_3 and δ-phase were obvious, but the intensity of the diffraction peaks of the matrix decreased.

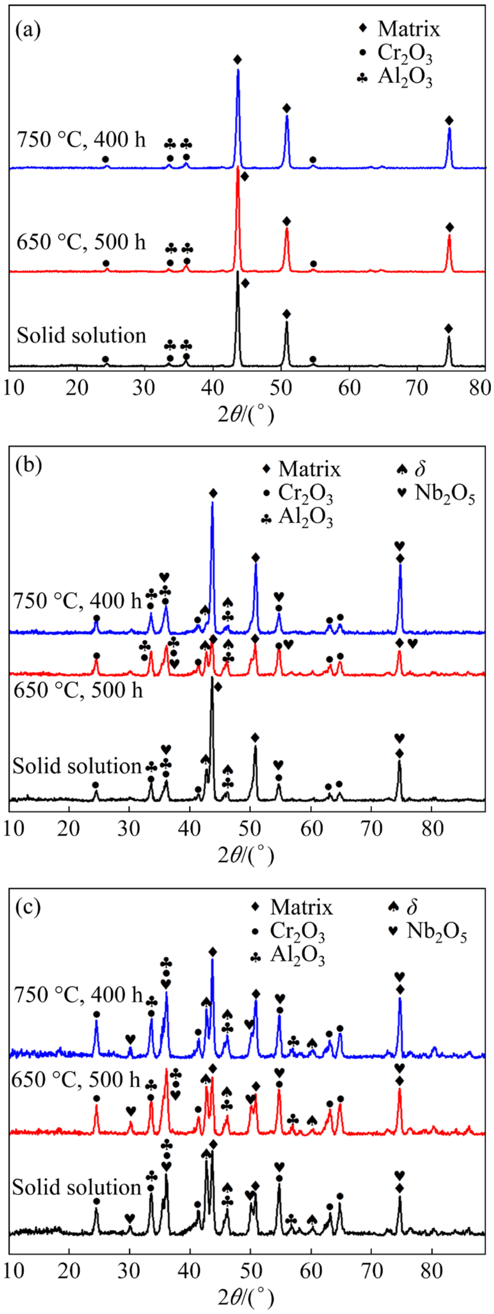

Fig. 3 XRD patterns of Inconel 625 alloy after oxidation at 950 °C for different time: (a) 1 h; (b) 24 h; (c) 200 h

3.4 Cross-sectional morphologies and elemental redistribution

To further clarify the structure of the oxide scale and the elemental composition of the Inconel 625 alloy after oxidation, the cross-sections of the three specimens were characterized. Figure 4(a) shows the cross-sectional morphology of the oxides of the solid-solution alloy after oxidation at 950 °C for 1 h. The surface of the alloy was covered with a thin oxide film, which was determined to be Cr-rich Cr_2O_3 based on the elemental composition of Point 1 (Table 3) in Fig. 4(a). A small amount of a particle-like internal oxide phase could be observed inside the matrix; this phase was determined to be Al-rich Al_2O_3 based on the elemental composition of Point 2 in Fig. 4(a) [13,21]. It is noteworthy that the Cr content of Point 2 is 18.6 at.%, which is higher than that of Al (10.1 at.%), and this phenomenon is due to the high Cr content in the alloy itself (21.71 wt.%), coupled with the insufficient magnification to resulting in a wide EDS point sweep area. The Cr content is much lower than that of Al, as can be clearly seen from Point 6 in Fig. 4(b).

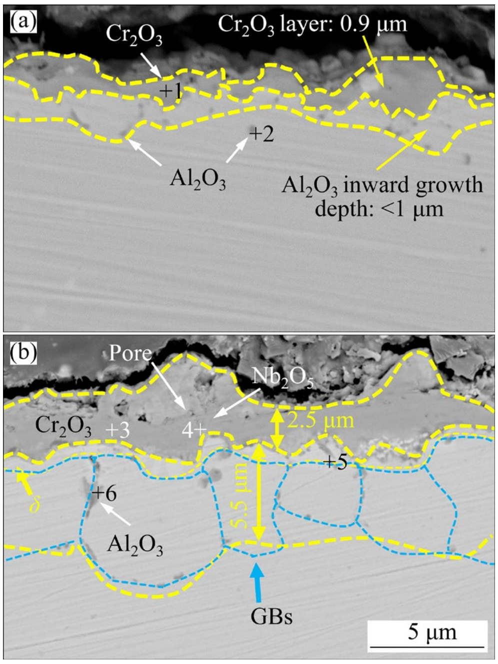

Fig. 4 Cross-sectional morphology of solid-solution alloy after oxidation at 950 °C for different time: (a) 1 h; (b) 24 h

Table 3 EDS results of each point in Fig. 4 (at.%)

Point	Ni	O	Cr	Nb	Mo	Ti	Al
1	2.3	57.9	36.8	2.4	0	0.6	0
2	50.1	17.3	18.6	2.7	1.2	0	10.1
3	1.04	56.8	41.4	0.48	0.1	0.1	0
4	4.7	52	14.6	27.6	0	0.6	0.4
5	66.3	7.5	4.1	20.4	1.4	0.2	0
6	44.4	20.6	3.7	9.9	0.7	0.1	20.5

Figure 4(b) shows the cross-sectional morphology of the oxidation products of the solid-solution alloy after oxidation at 950 °C for 24 h. Based on the EDS analysis results from Points 3 to

6, the oxide layer with a dark contrast on the surface of the alloy was determined to be Cr_2O_3. A small amount of bulk niobium-rich Nb_2O_5, which has a lighter contrast, was formed inside the Cr_2O_3 layer. The δ phase (Ni_3Nb) with a lighter contrast precipitated in the form of intermittent lamellae at the interface between the oxide layer and alloy matrix, as shown by the dotted line in Fig. 4(b). The precipitation of the δ phase is due to the diffusion of Cr and Nb to the surface of the alloy in the early stage of oxidation. A large amount of Cr reacted with oxygen in the air to form a Cr_2O_3 layer, resulting in the gathering of a large amount of Nb and Ni near the alloy surface, which promoted the precipitation of the δ phase [21]. The Al_2O_3 phase grew both in depth and in size, and its distribution characteristics also changed from a point-like distribution to chain-like distribution along the grain boundaries [13].

The cross-sections of the oxides of the solid-solution alloy of Inconel 625 were characterized by SEM after oxidation at 950 °C for 1, 24, 100, and 200 h to study the growth of the inner oxide and surface oxide layer (see Figs. 4 and 5). Figure 4(a) shows that Cr reacted with oxygen after oxidation for 1 h, and a single-phase Cr_2O_3 film was formed on the surface of the alloy with a thickness of 0.9 μm. Meanwhile, O element diffused into the alloy matrix and reacted with Al to form point-like Al_2O_3, and the Al_2O_3 inward growth depth was shallow (<1 μm).

Figure 4(b) shows the cross-sectional morphology of the Inconel 625 alloy after oxidation for 24 h. The thickness of the Cr_2O_3 layer increased significantly from 0.9 μm after 1 h to 2.5 μm after 24 h, and the outer oxide was still Cr_2O_3. The growth of the external oxide depends on the outward diffusion of Cr^{3+} to the alloy surface across the Cr_2O_3 layer and the inward diffusion of O^{2-} through the oxide layer. As the diffusion coefficient of Cr^{3+} in Cr_2O_3 is several orders of magnitude larger than that of O^{2-}, its outward diffusion led to the dominant growth of Cr_2O_3 [22]. The Al_2O_3 inward growth depth increased significantly to 5.5 μm, and its distribution also changed from point-like to chain-like distribution along the grain boundaries because of the higher energy at the grain boundary, which promoted the inward diffusion of O^{2-} [23].

Figures 5(a) and (b) show the cross-sectional morphology of Inconel 625 solid solution alloy oxidized at 950 °C for 100 and 200 h. The rate of oxidation of alloy after 24 h can be visualized from the rate of thickening. The thickness of the external

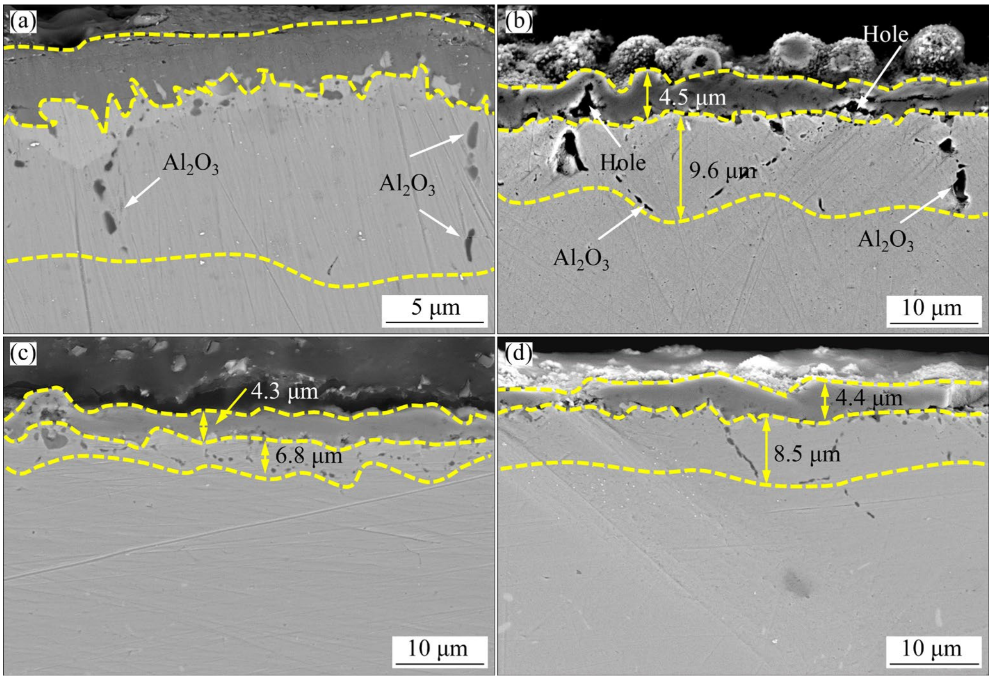

Fig. 5 Cross-sectional morphology of different heat treatment alloys after oxidation at 950 °C for different time: (a) Solid-solution alloy after oxidation for 100 h; (b) Solid-solution alloy after oxidation for 200 h; (c) Alloy oxidized for 200 h after aging at 650 °C for 500 h; (d) Alloy oxidized for 200 h after aging at 750 °C for 400 h

oxide layer (Cr_2O_3 layer) was increased to 4.5 μm, and the Al_2O_3 inward growth depth reached approximately 9.6 μm. In addition, a large number of holes were generated in the outer oxide layer, which is not conducive to the continuity and protective effect of the oxide layer.

The Pilling−Bedworth ratio (PBR) is the volume ratio of the oxide to metal required to form an oxide [24]. Generally, the larger the PBR value is, the greater the internal stress on the oxide is, which promotes crack initiation. When $1 < \mathrm{PBR} < 2$, the oxide plate is denser and exhibits excellent protection. At $\mathrm{PBR} > 2$, the compactness and continuity of the oxide film decrease significantly. The PBR value of Nb_2O_5 is approximately 2.6, which is the largest value for the oxidation products of the Inconel 625 alloy. The data of PBR values for some oxides are shown in Table 4. Therefore, Nb_2O_5 produces a large compressive stress during its formation and growth, resulting in the formation of pores near it, as shown in Fig. 4(b).

Table 4 PBR of some common oxides [25]

Oxide	MgO	V_2O_5	WO_3	Nb_2O_5	Cr_2O_3	Al_2O_3	NiO	TiO_2
PBR	0.81	3.19	3.3	2.6	2.07	1.38	1.65	1.73

Figures 5(c) and (d) illustrate the cross-sectional morphologies of the aged Inconel 625 alloys (ageing conditions: 650 °C, 500 h and 750 °C, 400 h) after oxidation at 950 °C for 200 h. The alloys subjected to different ageing treatments also contained the inner oxide product of Al_2O_3 and an outer layer of Cr_2O_3, as well as a large number of pores. The thickness of the Cr_2O_3 layer and the Al_2O_3 inward growth depth are listed in Table 5. There was almost no difference in the average thickness of the Cr_2O_3 layer in the different samples; however, the Al_2O_3 inward growth depth of the samples aged at 650 °C for 500 h and 750 °C for 400 h were significantly lower than that in the solid-solution alloy.

Table 5 Thickness of Cr_2O_3 layer and Al_2O_3 inward growth depth of alloys after oxidation at 950 °C for 200 h with different heat treatments

Heat treatment	Cr_2O_3 layer thickness/μm	Al_2O_3 inward growth depth/μm
Solution treatment	4.5±0.5	9.6±0.8
650 °C, 500 h	4.3±0.4	6.8±0.5
750 °C, 400 h	4.4±0.5	8.5±0.4

EPMA was used to study the elemental distribution and elemental diffusion behavior in the solid-solution alloy after high-temperature oxidation for 24 and 200 h. Figure 6 shows the cross-sectional morphology and EPMA elemental distribution of the solid-solution alloy after high-temperature oxidation at 950 °C for 24 h. The results indicate that O was mainly distributed on the surface of the alloy in the form of a dense Cr_2O_3 layer during the first 24 h of oxidation and then was distributed in the form of a chain of Al_2O_3 inside the matrix. Cr^{3+} continuously diffused to the surface of the alloy during high-temperature oxidation through the Cr_2O_3 film to the alloy surface to contact oxygen in the air, resulting in a depleted area of Cr near the surface of the substrate with a thickness of approximately 7 μm. In addition, Nb-enriched intermittent layered δ phase (Ni_3Nb) was observed at the interface between the oxide layer and substrate.

Figure 7 shows the cross-sectional morphology and EPMA distribution of the solid-solution alloy after high-temperature oxidation at 950 °C for 200 h. The oxidation products were still composed of Cr_2O_3 as an outer layer and inner chain-like Al_2O_3. With the increase of the oxidation time, Cr^{3+} continued to diffuse outward to generate Cr_2O_3, and the thickness of the Cr-depleted region near the substrate surface increased too. Figure 7(f) shows that the size and thickness of the layered Nb-enriched region increased, indicating an increase in the size and thickness of the δ phase.

Figures 8 and 9 show the cross-sectional morphology and EPMA elemental mapping of the oxide layer of Inconel 625 alloy oxidized for 200 h after ageing at 650 °C for 500 h and 750 °C for 400 h, respectively. Regardless of the ageing treatment method, the structure of the oxide layer of the alloy was not different from that of the solid-solution treated alloy, which is mainly composed of the outermost layer of Cr_2O_3 and the growth of Al_2O_3 into the matrix. There are some nickel signals outside the oxide layer, presumably introduced by the mounting press and fixed materials. The most significant difference is the depth of Al_2O_3 growth into the matrix, which is lower after aging than that after solid solution treatment, which is displayed in Table 5. It can be seen that the two aging treatments used in this work do not change the oxidation products and the structure of the oxide layer of

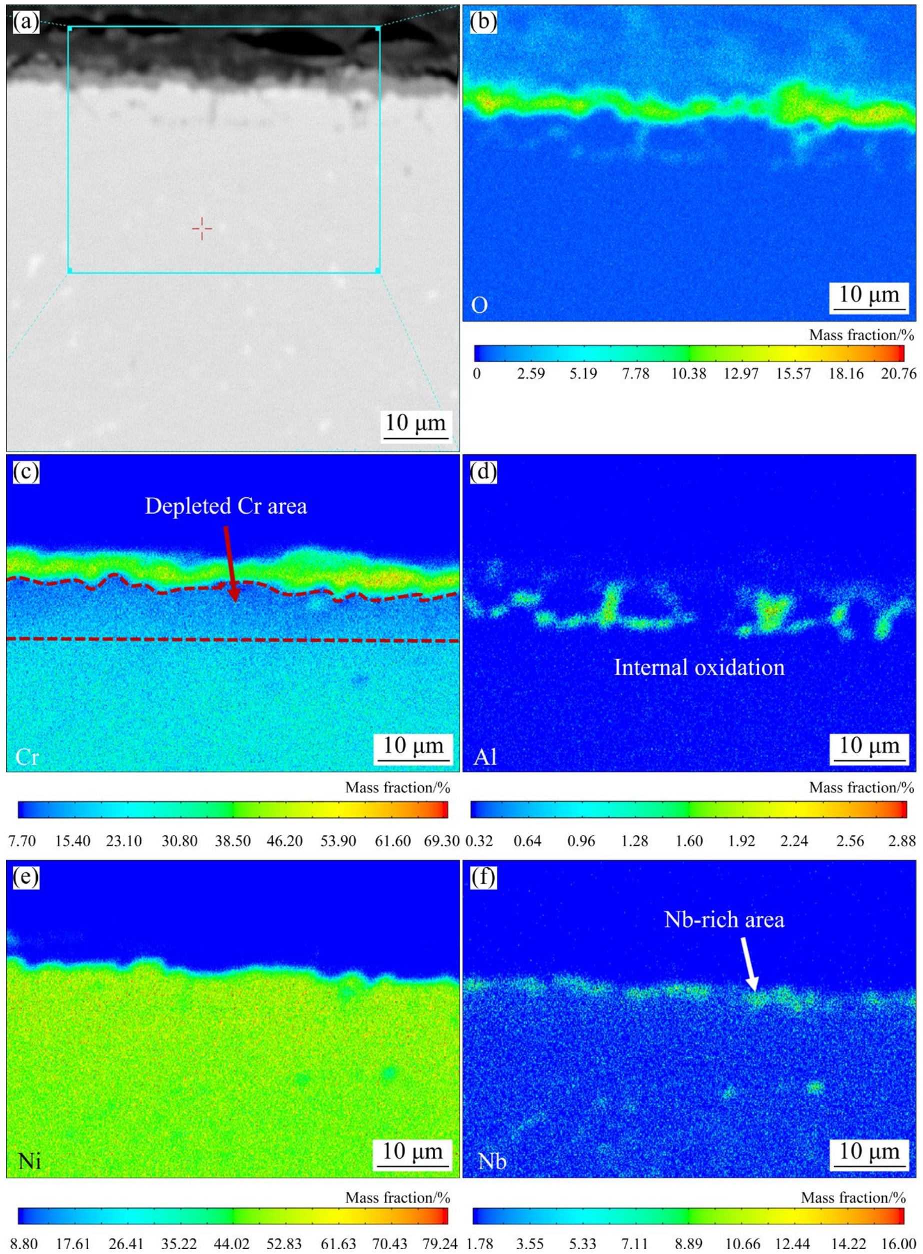

Fig. 6 Cross-sectional morphology of oxide layer and EPMA elemental mapping of solid-solution alloy of Inconel 625 after oxidation at 950 °C for 24 h: (a) SEM image; (b−f) EPMA elemental mapping of O, Cr, Al, Ni, and Nb respectively

Inconel 625 alloy, but only reduce the inward growth depth of Al_2O_3 and the inward diffusion depth of O^{2-}.

3.5 Morphology of surface oxide

Figure 10 shows the surface morphologies of alloys subjected to different heat treatments after oxidation at 950 °C for 1, 24, and 200 h. As shown, the oxide layer was relatively complete without peeling and provided good protection. The above analysis of the phase composition of the oxidation products revealed that the outer oxide of the alloy was uniquely Cr_2O_3. Figure 10 also shows that the morphologies of the surface oxidation products in the three samples were relatively similar after oxidation for 1 h. The surface of the alloy was covered by small granular oxides with gaps between the oxide particles. The Cr_2O_3 layer was formed by the direct contact of Cr on the surface with oxygen in the early stage of oxidation, and it covered the surface of the alloy relatively uniformly, thus playing a protective role. After 24 h of oxidation, the size of the oxide product increased, and the surface of the oxide layer became uneven.

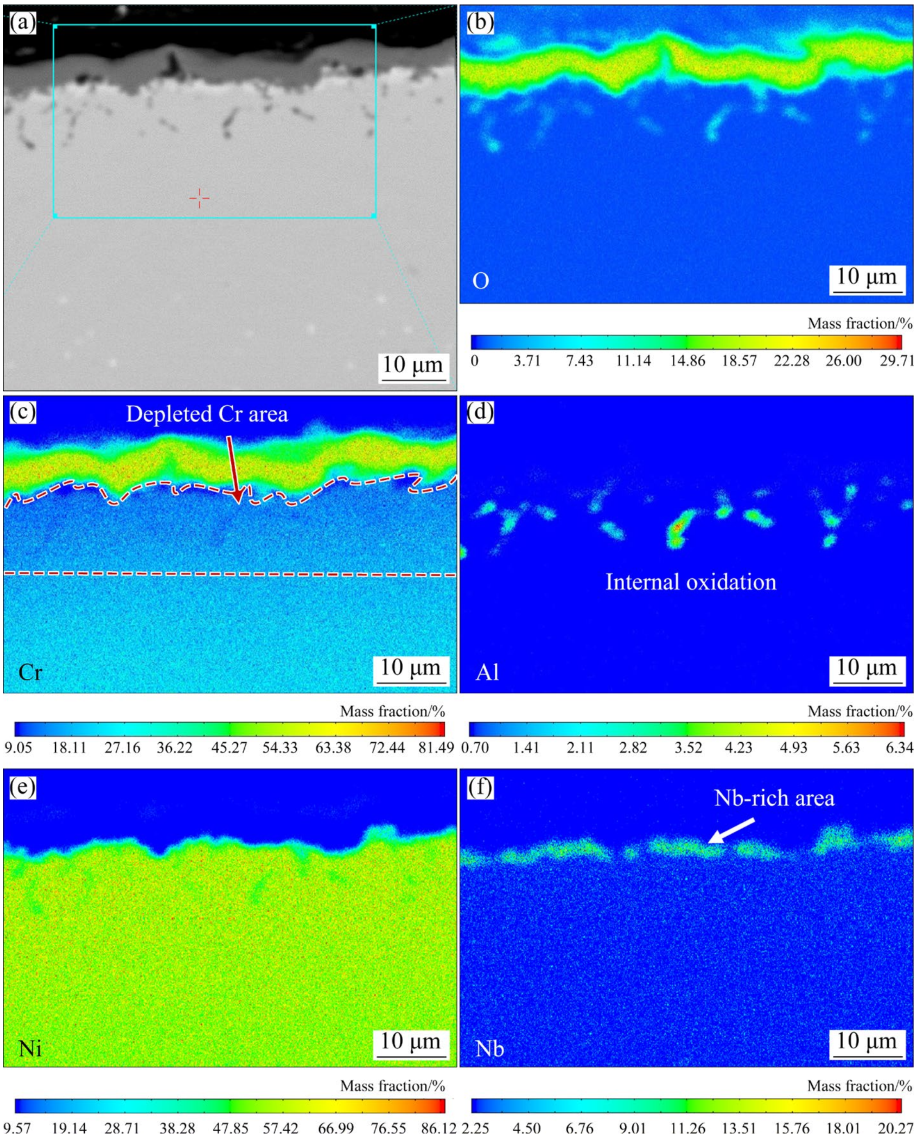

Fig. 7 Cross-sectional morphology of oxide layer and EPMA elemental mapping of solid-solution alloy of Inconel 625 after oxidation at 950 °C for 200 h: (a) SEM image; (b−f) EPMA elemental mapping of O, Cr, Al, Ni and Nb respectively

At the same time, the size of the oxide on the surface of the aged alloys was smaller. In addition, strip oxides appeared on the oxidized surface of the alloy after aging at 750 °C for 400 h (Figs. 10(c_2, c_3)). It is speculated that this particular shape of oxide is related to the needle-like δ phase in the matrix of the alloy after ageing treatment. They are similar in morphology and size, directly due to the special distribution of elements formed around the original δ phase. After 200 h of oxidation, the oxidation products on the surface of the alloys grew further, and the oxidation products of the solid-solution alloy grew into a nodular shape, while the oxide layer of the aged samples was relatively flat and dense, and provided better protection.

To better understand the formation mechanism of the surface oxidation products and the surface morphology, surface EPMA characterisation was performed on the solid-solution alloy and the specimen was treated at 750 °C for 400 h. Figure 11 shows the surface elemental distribution of the solid-solution specimen. The results reveal that Ni and Cr were uniformly distributed on the surface of the specimen, and Nb was only slightly aggregated. In contrast, the surface features of the specimen aged at 750 °C for 400 h indicated regional enrichment of Nb and Cr (Fig. 12). Owing to the

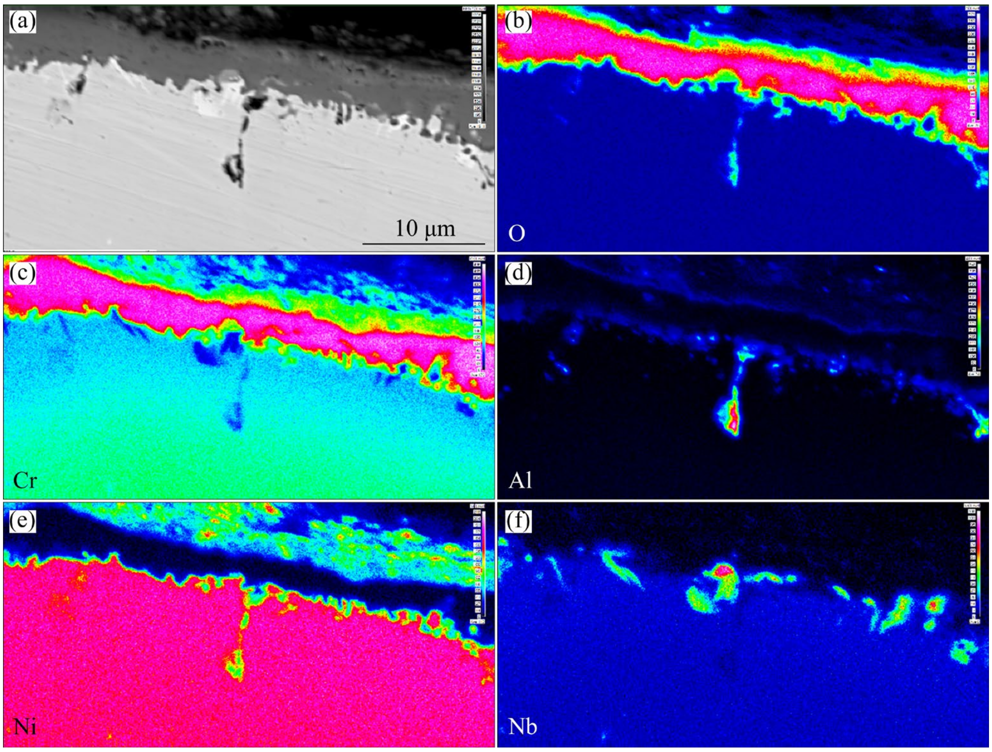

Fig. 8 Cross-sectional morphology and EPMA elemental mapping of oxide layer of Inconel 625 alloy oxidized for 200 h after ageing at 650 °C for 500 h: (a) SEM image; (b−f) EPMA elemental mapping of O, Cr, Al, Ni and Nb respectively

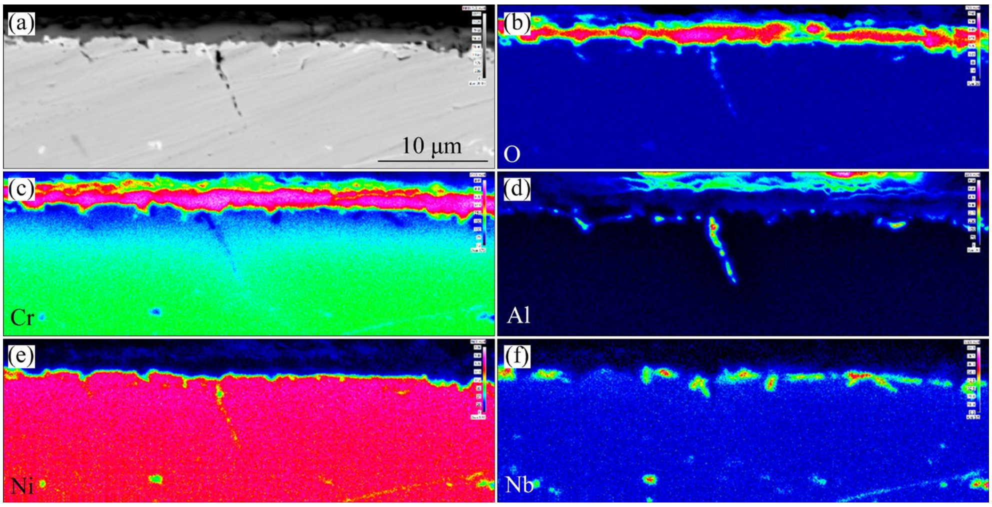

Fig. 9 Cross-sectional morphology and EPMA elemental mapping of oxide layer of Inconel 625 alloy oxidized for 200 h after ageing at 750 °C for 400 h: (a) SEM image; (b−f) EPMA elemental mapping of O, Cr, Al, Ni and Nb respectively

long ageing treatment, large amounts of γ'' and δ phases precipitated in the specimen.

The γ'' phase, which has the same chemical formula as the δ phase, is a disc-shaped metastable phase with an ordered tetragonal structure that precipitates at 550 °C. When the ageing temperature reaches 650 °C, the γ'' phase transforms into a steady-state needle-like ordered orthorhombic δ phase [26−28]. The generation of either phase causes the enrichment of Ni and Nb in this region, which in turn causes Cr enrichment around these two phases (Fig. 12). After both ageing treatments, Cr enrichment occurred on the alloy surface, and this enrichment provided compositional variations for the nucleation and growth of Cr_2O_3, resulting in a faster growth of Cr_2O_3 and more growth sites. The

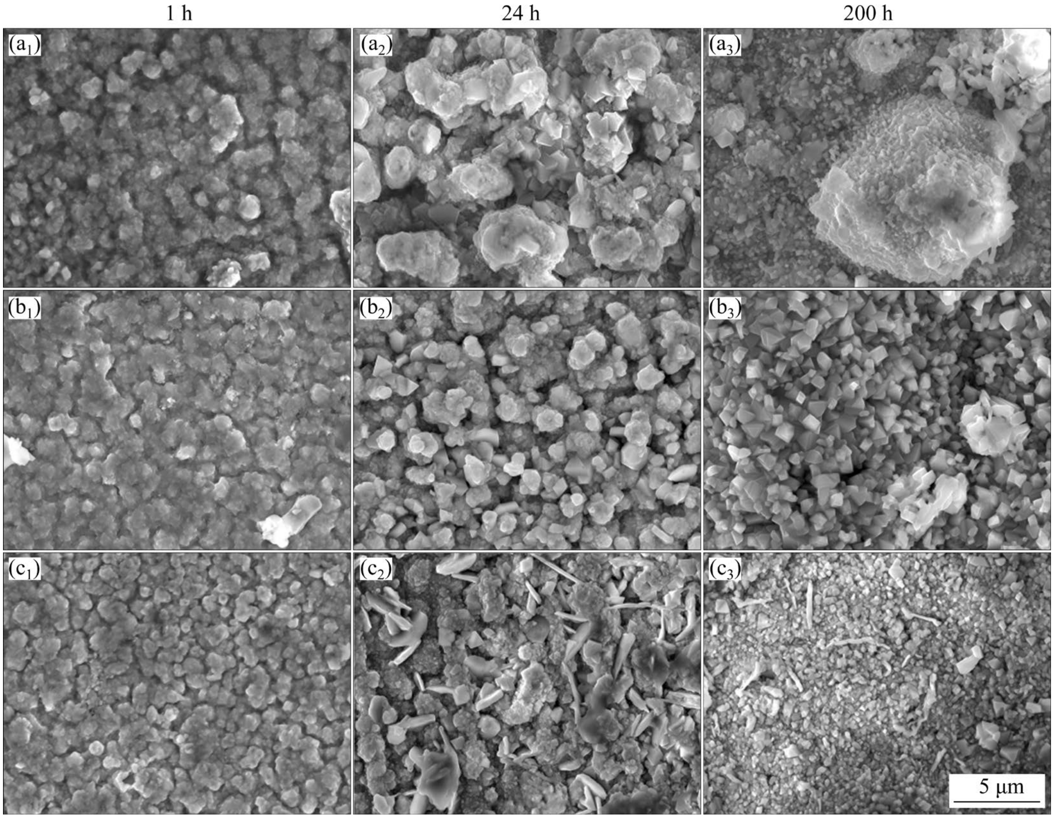

Fig. 10 Surface morphologies of alloys subjected to different heat treatments after 1, 24 and 200 h of oxidation: (a_1−a_3) Solid treatment; (b_1−b_3) Aged at 650 °C for 500 h; (c_1−c_3) Aged at 750 °C for 400 h

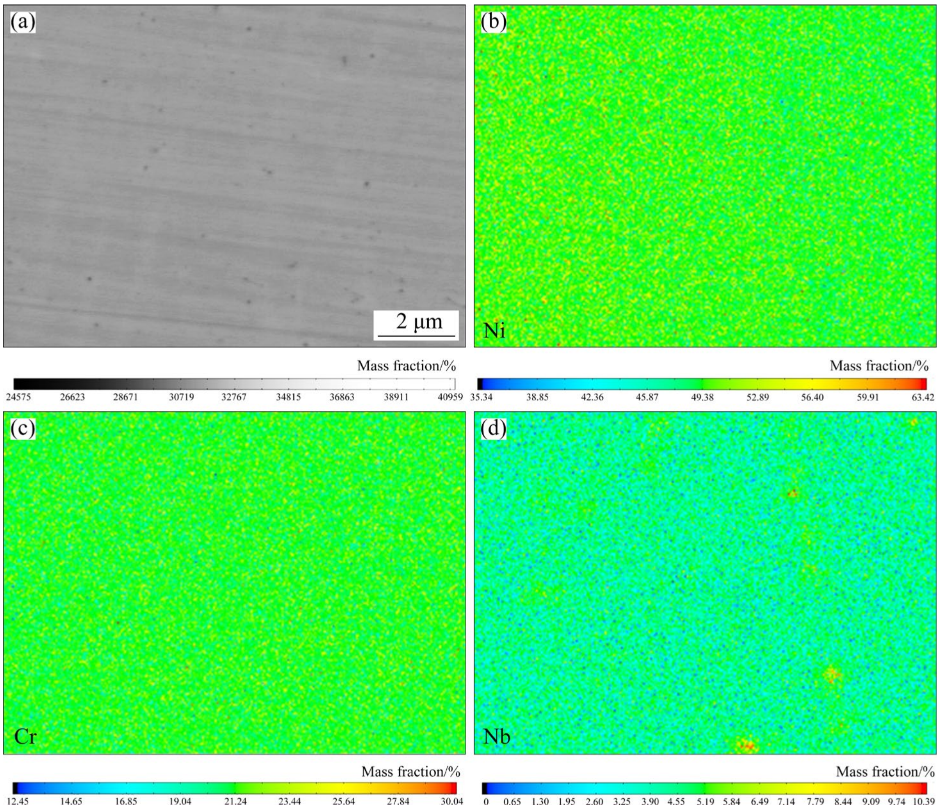

Fig. 11 Microstructure and EPMA elemental mapping of Inconel 625 alloy after solid solution treatments: (a) SEM image; (b−d) EPMA elemental mapping of Ni, Cr and Nb, respectively

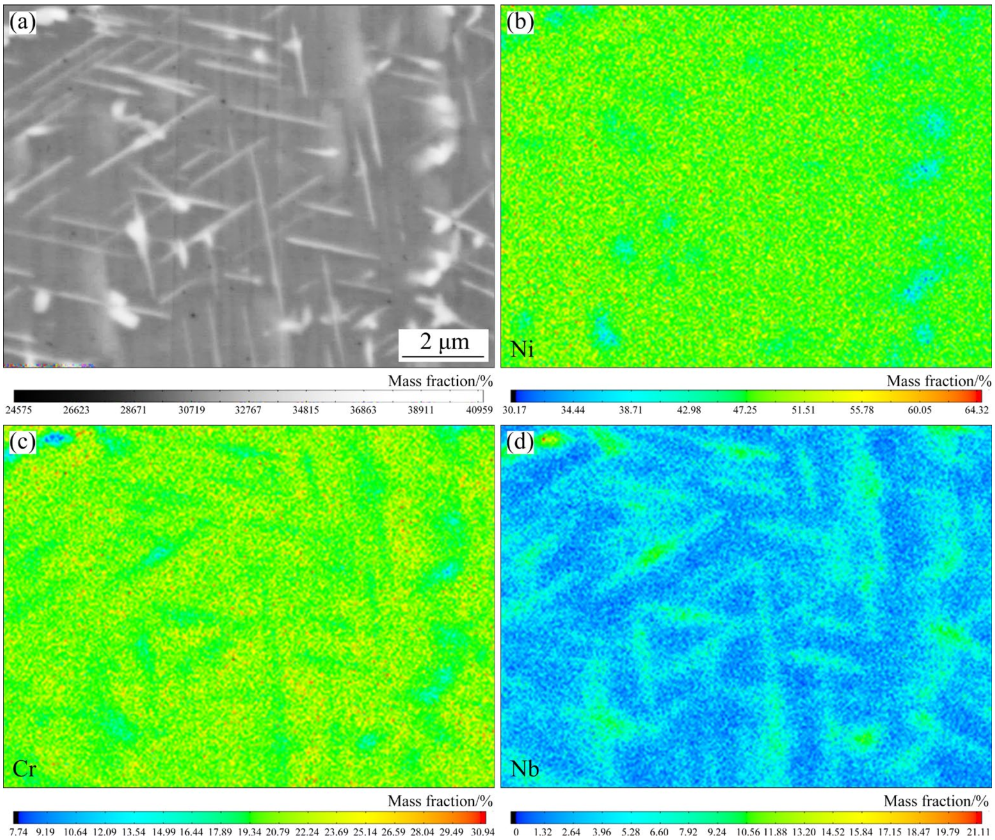

Fig. 12 Microstructure and EPMA elemental mapping of Inconel 625 alloy after ageing treatment at 750 °C for 400 h: (a) SEM image; (b−d) EPMA elemental mapping of Ni, Cr and Nb, respectively

fast-growing and denser Cr_2O_3 layer reduces the depth of O_2 diffusion into the matrix, leading to a reduction in Al_2O_3 inward growth depth, which improves the oxidation resistance of the Inconel 625 alloy.

3.6 Oxidation mechanism of Inconel 625 alloy

Different heat treatment processes change the oxidation behavior of Inconel 625 alloy, and it is essentially the phase structure and element distribution that bring about the oxidation behavior. The microstructures of Inconel 625 alloy under different heat treatments were characterized by SEM and TEM, and the results in Figs. 13(a) and (d) show the morphology of the alloy in the solid-solution state. The δ and γ'' phases are not observed in the alloy, and only carbides are found at the grain boundaries. Figures 13(b) and (e) show the morphology of the alloy after aging treatment at 650 °C for 500 h, and the disc-shaped γ'' phase is seen in the matrix. Figures 13(c) and (f) show the shape of the alloy after aging at 750 °C for 400 h, and the needle-like δ phase is present in the matrix.

The high-temperature oxidation mechanism of the Inconel 625 alloy can be illustrated in Fig. 14. For the sake of discussion, the whole oxidation process is described in two periods: the initial oxidation period and the later oxidation period. Figure 14(a) shows that Cr and Nb diffuse to the surface of the alloy during the initial oxidation period. Cr preferentially reacts with oxygen in the air and forms a Cr_2O_3 layer on the alloy surface. O diffuses into the matrix and reacts with Al in the matrix to form chain-like Al_2O_3. It is especially emphasized that abundant γ'' and δ phases exist in the matrix after aging treatment (Fig. 13). Obvious Cr enrichment was formed around these precipitates (Fig. 12), which resulted in the rapid formation of continuous and dense layers of Cr_2O_3 during the initial oxidation stage, preventing the inward diffusion of oxygen.

Figure 14(b) illustrates the later oxidation period of the alloy. The γ'' and δ phases in matrix have completely dissolved and disappeared at high temperatures. Cr diffuses to the interface between

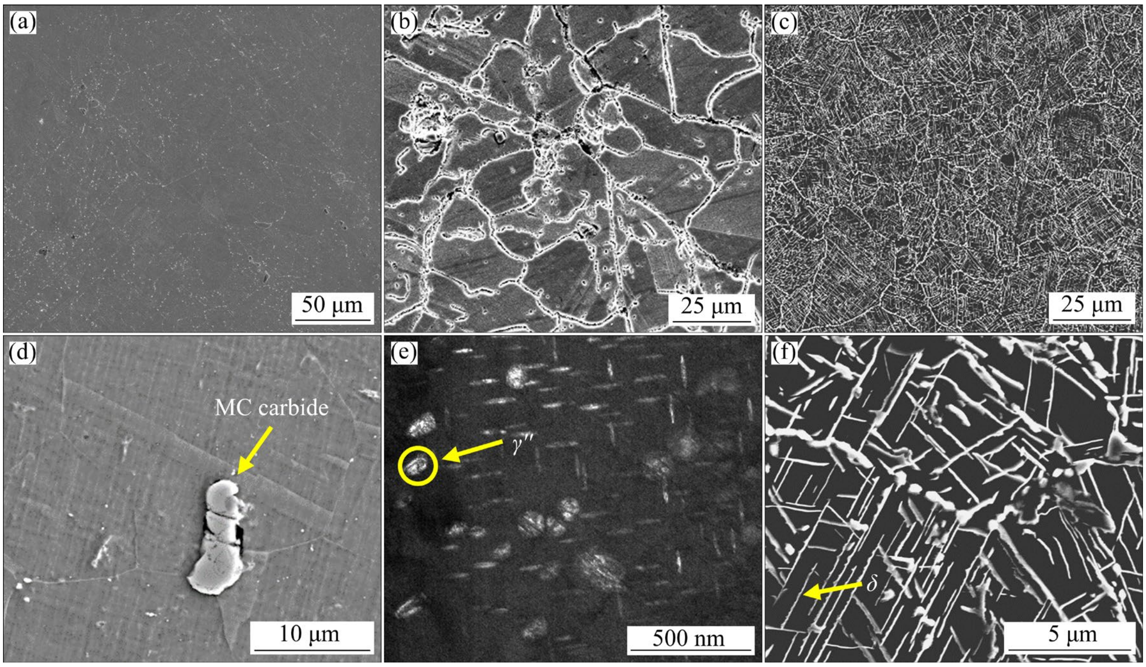

Fig. 13 Microstructures of Inconel 625 alloy in different heat treatment states: (a, d) Secondary electron image after solid-solution treatment; (b, e) Secondary electron image and transmitted dark field image after ageing treatment at 650 °C for 500 h; (c, f) Backscattered electron image after ageing treatment at 750 °C for 400 h

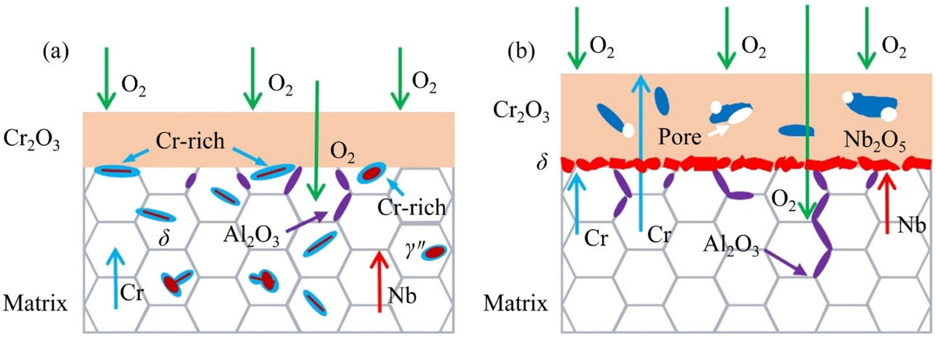

Fig. 14 Schematic diagram of 950 °C oxidation mechanism of aged Inconel 625 alloy: (a) Initial oxidation period; (b) Later oxidation period

the alloy and oxide layer in this stage, and reacts with the inward diffused O to form Cr_2O_3. Meanwhile, Cr diffuses further through the oxide film to the surface of the alloy and contacts with oxygen to form Cr_2O_3, resulting in a continuous increase in the thickness of the Cr_2O_3 layer. The generation of stable and thickening Cr_2O_3 is mainly due to the high content of Cr in the alloy (21.71 wt.%) and the relatively low Gibbs free energy change for the oxidation reaction of Cr (lower than that of Ni, which is more abundant in the alloy). Nb diffuses to the interface between the alloy and oxide layer to precipitate as an intermittent-layered δ phase (Ni_3Nb), resulting in the formation of an enriched area of Ni and Nb near the interface. Nb also diffuses into the Cr_2O_3 layer to generate Nb_2O_5, and its precipitation leads to the generation of pores and destruction of the continuity of the oxide layer. O continuously diffuses into the matrix, and the grain boundary provides a fast channel for the inward diffusion of oxygen. Therefore, O preferentially reacts with Al at the grain boundary to form chain-like Al_2O_3.

4 Conclusions

(1) The oxidation mass gain of the alloys subjected to ageing treatment at 650 °C for 500 h and at 750 °C for 400 h was lower than that of the solid-solution Inconel 625 alloy, indicating that the

ageing treatment could improve the oxidation resistance of the alloy.

(2) The oxide layer of the alloy mainly consists of an outer layer of Cr_2O_3 and an inner layer of chain-like Al_2O_3 distributed along grain boundaries. In addition, an intermittent layer of δ-phase is generated at the interface between the Cr_2O_3 layer and the substrate during the oxidation process, and a small amount of massive Nb_2O_5 precipitates inside the Cr_2O_3 layer as the oxidation proceeds.

(3) The ageing treatment did not significantly change the thickness of the Cr_2O_3 layer but reduced the Al_2O_3 inward growth depth of the alloy.

(4) The ageing treatment caused the precipitation of γ'' and δ phases in the Inconel 625 alloy, resulting in the enrichment of Cr near the two phases. The enrichment of Cr caused the rapid generation of a dense Cr_2O_3 layer on the surface, which prevented the diffusion of oxygen into the matrix, reduced the Al_2O_3 inward growth depth, and improved the oxidation resistance of the alloy.

CRediT authorship contribution statement

Jiang-kun FAN, **Hong-ci YANG** and **Pei-zhe ZHANG:** Investigation, Writing − Original draft, Visualization, Formal analysis, Data curation; **Jia-yu LI**, **Zhan-jie JING**, **Fu-long CHEN** and **De-gui LIU:** Investigation, Methodology; **Bin TANG** and **Hong-chao KOU:** Data curation, Writing − Review & editing; **Jin-shan LI:** Supervision, Funding acquisition.

Declaration of competing interest

The authors declare that they have no known competing financial interests or personal relationships that could have appeared to influence the work reported in this paper.

Acknowledgments

This work was financially supported by the National Science and Technology Major Project of China (Nos. MJ-2018-G-48, J2019-VI-0023-0140), and the Research Fund of the State Key Laboratory of Solidification Processing (NPU), China (No. 2022-TS-04).

References

[1] FRIEND W Z, COHEN M. Corrosion of nickel and nickel-base alloys [J]. Journal of the Electrochemical Society, 1980, 127: 421C.

[2] LIU Xu-dong, FAN Jiang-kun, SONG Yue-lin, ZHANG Pei-zhe, CHEN Fu-long, YUAN Rui-hao, WANG Jun, TANG Bin, KOU Hong-chao, LI Jin-shan. High-temperature tensile and creep behaviour of Inconel 625 superalloy sheet and its associated deformation-failure micromechanisms [J]. Materials Science and Engineering A, 2022, 829: 142152.

[3] SAFARZADE A, SHARIFITABAR M, SHAFIEE AFARANI M. Effects of heat treatment on microstructure and mechanical properties of Inconel 625 alloy fabricated by wire arc additive manufacturing process [J]. Transactions of Nonferrous Metals Society of China, 2020, 30: 3016−3030.

[4] REED R C. The superalloys: Fundamentals and applications [M]. Cambridge: Cambridge University Press, 2008.

[5] GAO Yu-bi, DING Yu-yian, CHEN Jian-jun, XU Jia-yu, MA Yuan-jun, WANG Xing-mao. Effect of twin boundaries on the microstructure and mechanical properties of Inconel 625 alloy [J]. Materials Science and Engineering A, 2019, 767: 138361.

[6] GAO Yu-bi, LI Xiu-yan, MA Yuan-jun, KITCHEN M, DING Yu-tian, LUO Quan-shun. Formation mechanism and wear behavior of gradient nanostructured Inconel 625 alloy [J]. Transactions of Nonferrous Metals Society of China, 2022, 32: 1910−1925.

[7] PEI Hai-qing, WEN Zhi-xun, YUE Zhu-feng. Long-term oxidation behavior and mechanism of DD6 Ni-based single crystal superalloy at 1050 °C and 1100 °C in air [J]. Journal of Alloys and Compounds, 2017, 704: 218−226.

[8] QIN Lu, PEI Yan-ling, LI Shu-suo, ZHAO Xin-bao, GONG Sheng-kai, XU Huai-bin. Role of volatilization of molybdenum oxides during the cyclic oxidation of high-Mo containing Ni-based single crystal superalloys [J]. Corrosion Science, 2017, 129: 192−204.

[9] PARIZIA S, MARCHESE G, RASHIDI M, LORUSSO M, HRYHA E, MANFREDI D, BIAMINO S. Effect of heat treatment on microstructure and oxidation properties of Inconel 625 processed by LPBF [J]. Journal of Alloys and Compounds, 2020, 846: 156418.

[10] JANG C, KIM D, KIM D, SAH I, RYU Woo-seog, YOO Young-sung. Oxidation behaviors of wrought nickel-based superalloys in various high temperature environments [J]. Transactions of Nonferrous Metals Society of China, 2011, 21: 1524−1531.

[11] VESEL A, DRENIK A, ELERSIC K, MOZETIC M, KOVAC J, GYERGYEK T, STOCKEL J, VARJU J, PANEK R, BALAT-PICHELIN M. Oxidation of Inconel 625 superalloy upon treatment with oxygen or hydrogen plasma at high temperature [J]. Applied Surface Science, 2014, 305: 674−682.

[12] SHARIFITABAR M, KHORSHAHIAN S, AFARANI M S, KUMAR P, JAIN N K. High-temperature oxidation performance of Inconel 625 superalloy fabricated by wire arc additive manufacturing [J]. Corrosion Science, 2022, 197: 110087.

[13] CHYRKIN A, HUCZKOWSKI P, SHEMET V, SINGHEISER L, QUADAKKERS W J. Sub-scale depletion and enrichment processes during high temperature oxidation of the nickel base alloy 625 in the temperature range 900−1000 °C [J]. Oxidation of Metals, 2011, 75: 143−166.

[14] ELLINGHAM H. Reducibility of oxides and sulphides in metallurgical processes [J]. Journal of the Chemical Society,

1944, 63: 125−160.

[15] SUN Yu-zhou, CHEN Lan, LI Lin, REN Xu-dong. High-temperature oxidation behavior and mechanism of Inconel 625 super-alloy fabricated by selective laser melting [J]. Optics & Laser Technology, 2020, 132: 106509.

[16] SADEGHI E, KARIMI P, MOMENI S, SEIFI M, EKLUND A, ANDERSSON J. Influence of thermal post treatments on microstructure and oxidation behavior of EB-PBF manufactured Alloy 718 [J]. Materials Characterization, 2019, 150: 236−251.

[17] LIANG Zhen-quan, XIAO Shu-long, YUE Hang-yu, LI Xin-yi, LI Qing-chao, ZHENG Yun-fei, XU Li-juan, XUE Xiang, TIAN Jing, CHEN Yu-yong. Tailoring microstructure and improving oxidation resistance of an additively manufactured high Nb containing TiAl alloy via heat treatment [J]. Corrosion Science, 2023, 220: 111287.

[18] TIAN Shi-wei, HE An-rui, LIU Jian-hua, ZHANG Ye-fei, YANG Yong-gang, ZHANG Yun, JIANG Hai-tao. Oxidation resistance of TiAl alloy improved by hot-pack rolling and cyclic heat treatment [J]. Materials Characterization, 2021, 178: 111196.

[19] HASEGAWA M. Ellingham diagram [M]//Treatise on Process Metallurgy. Amsterdam: Elsevier, 2014: 507−516.

[20] ZHENG Lei, ZHANG Mai-cang, DONG Jian-xin. Oxidation behavior and mechanism of powder metallurgy Rene95 nickel-based superalloy between 800 and 1000 °C [J]. Applied Surface Science, 2010, 256: 7510−7515.

[21] de SOUSA MALAFAIA A M, de OLIVEIRA R B, LATU-ROMAIN L, WOUTERS Y, BALDAN R. Isothermal oxidation of Inconel 625 superalloy at 800 and 1000 °C: Microstructure and oxide layer characterization [J]. Materials Characterization, 2020, 161: 110160.

[22] YANG Z, LU J T, YANG Z, LI Y, YUAN Y, GU Y F. Oxidation behavior of a new wrought Ni−30Fe−20Cr based alloy at 750 °C in pure steam and the effects of alloyed yttrium [J]. Corrosion Science, 2017, 125: 106−113.

[23] WELSCH G, DESAI P D. Oxidation and corrosion of intermetallic alloys [R]. Purdue University, 1996.

[24] PILLING N, BEDWORTH B. The oxidation of metals at high temperatures [J]. Journal of the Institute of Metals, 1923, 29: 529−582.

[25] LI Mei-shuang, QIAN Yu-hai, XIN Li. Volume ratio of an oxide to the metal [J]. Corrosion Science and Protection Technology, 1997, 5: 284−289.

[26] SUAVE L M, CORMIER J, VILLECHAISE P, SOULA A, HERVIER Z, BERTHEAU D, LAIGO J. Microstructural evolutions during thermal aging of alloy 625: Impact of temperature and forming process [J]. Metallurgical and Materials Transactions A, 2014, 45: 2963−2982.

[27] SUNDARARAMAN M, MUKHOPADHYAY P, BANERJEE S. Precipitation of the δ-Ni_3Nb phase in two nickel base superalloys [J]. Metallurgical Transactions A, 1988, 19: 453−465.

[28] GARCIA-FRESNILLO L, CHYRKIN A, BÖHME C, BARNIKEL J, SCHMITZ F, QUADAKKERS W J. Oxidation behaviour and microstructural stability of alloy 625 during long-term exposure in steam [J]. Journal of Materials Science, 2014, 49: 6127−6142.

不同固溶时效热处理状态 Inconel 625 合金的高温氧化机理

樊江昆[1,2,3]，杨洪赐[1]，张沛喆[1]，李佳煜[1]，景战杰[1]，
陈福龙[1,4]，刘德贵[4]，唐 斌[1,2,3]，寇宏超[1,2,3]，李金山[1,2,3]

1. 西北工业大学 凝固技术国家重点实验室，西安 710072；
2. 先进金属材料精确热成型技术国家地方联合工程研究中心，西安 710072；
3. 西北工业大学 重庆科创中心，重庆 401135；
4. 中国航空制造技术研究院，北京 100024

摘 要：研究经过不同时效处理后 Inconel 625 合金在 950 ℃下的高温氧化行为。通过分析氧化前后合金的结构和元素分布特征，研究热处理对合金氧化行为的影响。结果表明，两种时效处理(650 ℃，500 h 和 750 ℃，400 h)都减小了合金氧化后的质量变化。在 950 ℃下氧化后，外层 Cr_2O_3 和内层 Al_2O_3 为主要氧化产物。此外，氧化后还会析出 Nb_2O_5 和 δ(Ni_3Nb)相。时效处理使合金表面迅速生成致密的 Cr_2O_3 层，阻止氧气向基体的扩散，降低 Al_2O_3 向内生长的深度，提高合金的抗氧化性。

关键词：Inconel 625 合金；时效处理；氧化行为；氧化膜；动力学

(Edited by Xiang-qun LI)